PHYSICAL REVIEW B **94**, 155144 (2016)

Laser angle-resolved photoemission as a probe of initial state k_z dispersion, final-state band gaps, and spin texture of Dirac states in the Bi_2Te_3 topological insulator

Minna Ärrälä,[1] Hasnain Hafiz,[2] Daixiang Mou,[3,4] Yun Wu,[3,4] Rui Jiang,[3,4] Trevor Riedemann,[4] Thomas A. Lograsso,[4,5] Bernardo Barbiellini,[2] Adam Kaminski,[3,4] Arun Bansil,[2] and Matti Lindroos[1,2,*]

[1]*Institute of Physics, Tampere University of Technology, P.O. Box 692, FIN-33101 Tampere, Finland*

[2]*Department of Physics, Northeastern University, Boston, Massachusetts 02115, USA*

[3]*Department of Physics and Astronomy, Iowa State University, Ames, Iowa 50011, USA*

[4]*Division of Materials Science and Engineering, Ames Laboratory, Ames, Iowa 50011, USA*

[5]*Materials Science and Engineering Department, Iowa State University, Ames, Iowa 50011, USA*

(Received 6 July 2016; published 27 October 2016)

We have obtained angle-resolved photoemission spectroscopy (ARPES) spectra from single crystals of the topological insulator material Bi_2Te_3 using a tunable laser spectrometer. The spectra were collected for 11 different photon energies ranging from 5.57 to 6.70 eV for incident light polarized linearly along two different in-plane directions. Parallel first-principles, fully relativistic computations of photointensities were carried out using the experimental geometry within the framework of the one-step model of photoemission. A reasonable overall accord between theory and experiment is used to gain insight into how properties of the initial- and final-state band structures as well as those of the topological surface states and their spin textures are reflected in the laser-ARPES spectra. Our analysis reveals that laser-ARPES is sensitive to both the initial-state k_z dispersion and the presence of delicate gaps in the final-state electronic spectrum.

DOI: 10.1103/PhysRevB.94.155144

I. INTRODUCTION

Topological insulators (TIs) [1] have continued to draw intense interest since their discovery a few years ago [2–14]. Bismuth-based binary compounds (Bi_2Te_3 and Bi_2Se_3) were the first materials predicted to host the three-dimensional (3D) TI phase, which was subsequently verified experimentally. The nontrivial band topology of Bi_2Te_3 and Bi_2Se_3 is controlled by the inversion of Bi and Te p orbitals under the effects of spin-orbit coupling. The great current interest in the TIs stems from their novel electronic structures in that even though the bulk of these materials is insulating, the surfaces of a 3D TI and edges of a 2D TI are guaranteed to host gapless topological surface states (TSSs), which are protected by constraints of time-reversal symmetry against nonmagnetic perturbations. The TSSs in TIs exhibit a Dirac-cone-like linear energy-momentum dispersion and feature unique spin-momentum locking properties, which make the TIs attractive for developing a new generation of materials platform for investigating fundamental phenomena as well as spintronics and other applications.

Angle-resolved photoemission spectroscopy (ARPES) has been used widely for investigating the bulk as well as the topological surface states in the TIs. Accessing spin textures of the TSSs via spin-resolved ARPES (SARPES), on the other hand, has generally proven to be more challenging. For example, circular-dichroism ARPES (CD-ARPES) experiments, where one measures the difference in ARPES intensities for right- and left-circularly polarized light, show that the CD-ARPES spectrum changes sign with photon energy from the same sample of a Bi_2Te_3 single crystal, making it clear that CD-ARPES cannot provide a probe of the initial-state spin structure [15–17]. These results are not surprising since it is well known that spectral intensities in highly resolved spectroscopies such as ARPES depend sensitively on matrix element effects, which in the case of ARPES involve not only the properties of the initial-state but also of the final-state wave functions [18–20].

In this study, we examine the role of the ARPES matrix element in laser-ARPES spectra from TIs and delineate how the imprints of the Dirac states and their spin textures are encoded in these spectra in terms of the characters and symmetries of the initial and final states. For this purpose, we collected laser-ARPES spectra from the exemplar TI material Bi_2Te_3 over a wide range of momenta in the $k_x - k_y$ plane at energies ranging from 5.57–6.70 eV for two different linear polarizations of the incident light. The experimental results are analyzed in terms of the corresponding first-principles computations of ARPES intensities, which were carried out within the framework of the one-step model of photoemission, and include effects of the ARPES matrix element from a semi-infinite solid surface. In this way, we obtain insights into the nature of the laser-ARPES spectra from TIs, and how these spectra contain fingerprints of the initial-state k_z dispersions, spin textures of the Dirac cone states, and provide a window into the presence of delicate gaps in the final-state spectrum.

II. COMPUTATIONS

ARPES intensities were computed fully relativistically within the framework of the one-step model [21–23]. As in our previous laser-ARPES studies, we chose a small value of the imaginary part, $\Sigma_f'' = 0.1$ eV (full width at half maximum of 0.2 eV), for the final-state self-energy [15–17]. This value of Σ_f'' is comparable to the value of 0.2 eV for low photon energies suggested by Strocov *et al.* [24]. Note that at these low photon energies, we are below the threshold for plasmon excitations, which would substantially add to the

*matti.lindroos@tut.fi

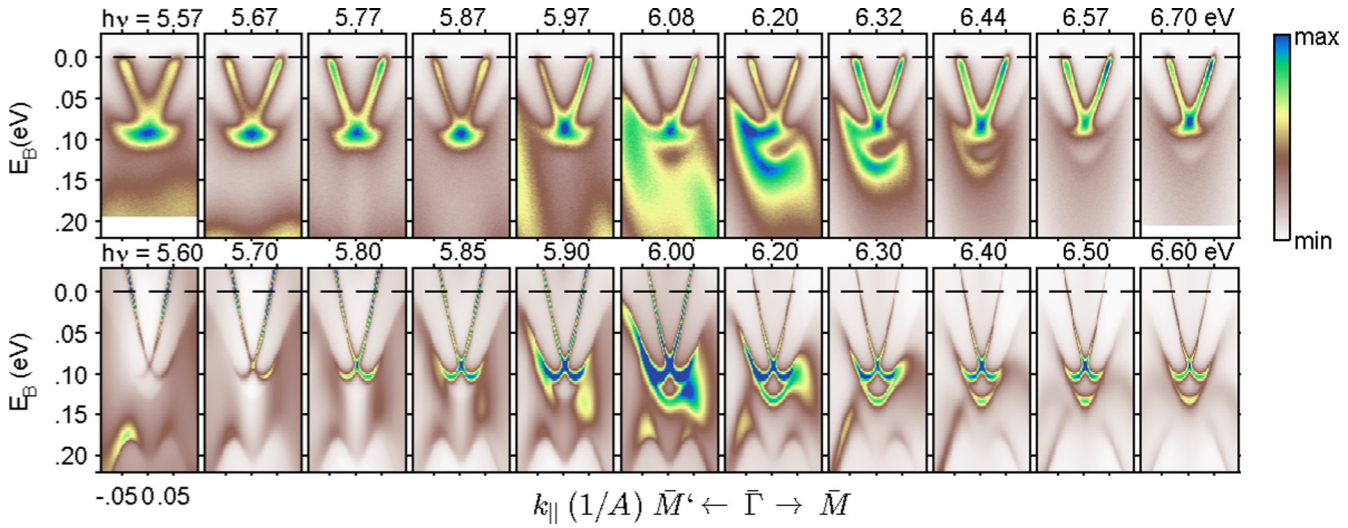

FIG. 1. Top row: Experimental laser-ARPES spectra over the photon energy range of 5.57–6.70 eV from a Bi_2Te_3 single crystal. Spectra are shown as a function of the initial-state binding energy and momentum taken along a direction which is misaligned by 5° with respect to the $\bar{\Gamma}\bar{M}$ direction. The incoming light is propagating along $\bar{\Gamma}\bar{K}$, and it is p polarized with a polar angle of 50°. All spectra are normalized to the maximum in each panel as shown. Bottom row: Corresponding theoretical intensities computed within the one-step model, normalized in each panel as shown; experimental conditions of light polarization and misalignment of the sample have been taken into account in the computations.

damping of final states. Also, we find that the rapid changes in spectral intensity with photon energy, which are observed experimentally, are washed out when we use values of $\Sigma_f{}''$ larger than 0.3 eV. Although the underlying crystal potential in our photointensity computations is of the muffin-tin form, this potential essentially reproduces the first-principles bulk and surface states of interest in this study. For the initial-state self-energy, $\Sigma_i{}'' = 5$ meV was chosen in order to better highlight and interpret initial-state features in the spectra. An ideal Te-terminated surface was assumed. For further details of our methodology for ARPES computations, we refer the reader to our earlier publications [15–20,25,26].

III. EXPERIMENTS

Single crystals were grown using the proper ratio of high-purity bismuth (99.999%) and tellurium (99.999%) metals that were sealed in a quartz tube and melted into an ingot in an induction furnace to homogenize the composition. The ingot was then sealed in a quartz tube with a larger diameter and loaded into a Bridgman furnace. A single crystal was grown by withdrawing the quartz tube at 1 mm/hr after it was heated to 800 °C. The chemical composition of the sample was confirmed using electron-probe microanalysis (EPMA).

Samples were cleaved *in situ* at a base pressure lower than 8×10^{-11} Torr. ARPES measurements were carried out using a laboratory-based system consisting of a Scienta R8000 electron analyzer and a tunable VUV laser light source. ARPES spectra were acquired over the photon energy range from 5.57 to 6.7 eV. The energy resolution of the analyzer was set at 1 meV, while the angular resolution was 0.13° and ∼0.5° along and perpendicular to the direction of the analyzer slits, respectively. Samples were cooled using a closed-cycle He refrigerator. Temperature was measured using a silicon-diode sensor mounted on the sample holder. The energy corresponding to the chemical potential was determined from the Fermi edge of a polycrystalline Au reference in electrical contact with the sample. The aging effect was checked by recycling measurements. The consistency of the data was confirmed by measuring several samples.

IV. RESULTS AND DISCUSSION

Figure 1 compares the experimental ARPES intensities along the $\bar{\Gamma}\bar{M}$ direction (top row) with the corresponding theoretical results (bottom row) over a range of photon energies, and shows that our computations capture a number of characteristic features of the measured spectra [27]. The intensity pattern is expected to be asymmetric around $\bar{\Gamma}$ due to the geometry of the system, as is seen to be the case in both theory and experiment. The spectral intensity coming from the bulk bands shows an interesting pattern in the measurements: As we go from the left to the right in the top row, at the lowest photon energy (5.57 eV), there is considerable bulk intensity below the Dirac node; this intensity moves to a lower binding energy at 5.67 eV and disappears by 5.77 eV. The bulk intensity then begins to reappear and becomes quite substantial by 5.97 eV and overlaps the nodal region for higher photon energies, although the related intensity becomes quite weak once again by 6.70 eV. Evolution of the theoretical spectra with photon energy in the bottom row of Fig. 1 follows this observed behavior to a remarkable level, some differences in details notwithstanding.

In order to gain insight into the preceding results, we discuss with reference to Fig. 2 how the behavior of the spectral peaks in the ARPES spectra is connected with the energy dispersions of the initial- and final-state bands. Figure 2(a) shows the computed energy distribution curves (EDCs) for $h\nu$ varying from 5.5 to 12.9 eV for the fixed value of $k_{\|} = k_F$, i.e., the momentum point where the Dirac cone intersects the E_F along

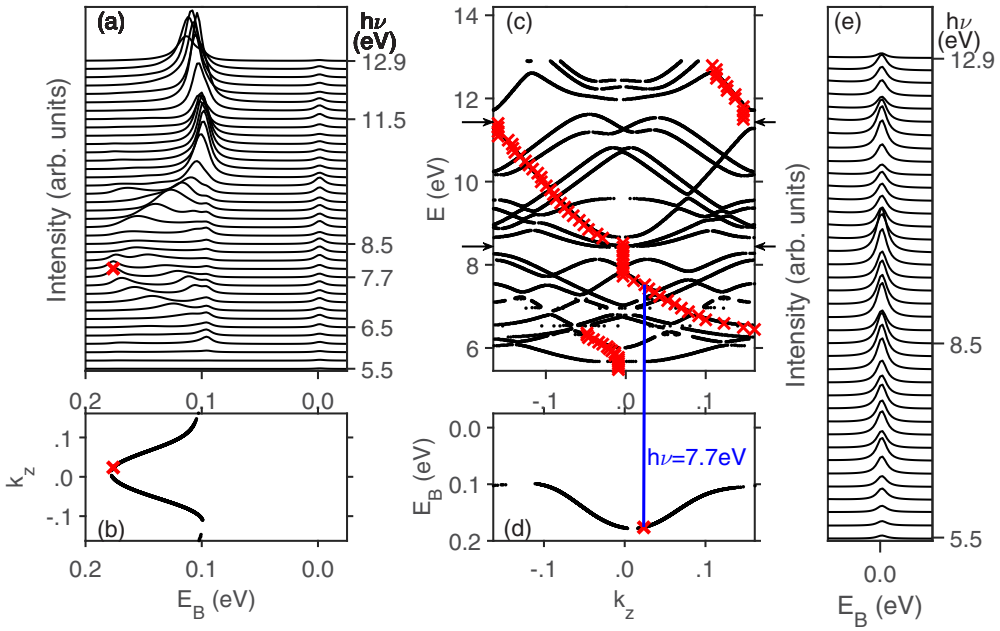

FIG. 2. (a) Theoretical energy distribution curves (EDCs) for photon energies ($h\nu$) varying from 5.5 to 12.9 eV, giving photointensity as a function of the initial-state binding energy, with $k_\parallel$ held fixed at the Fermi momentum k_F along the $\bar{\Gamma}\bar{M}$ direction. The initial and final states associated with the peaks in the EDCs are clarified in panels (b)–(d) by considering the example of the peak marked by a red cross on the EDC for $h\nu = 7.7$ eV. (b) k_z dispersion of the initial (bulk) state associated with the spectral peaks in the EDC for $k_\parallel = k_F$. k_z value corresponding to the peak marked with a cross is identified. (c) k_z dispersion of the final (bulk) states. Note that k_z is given on the horizontal scale, while the vertical scale gives the final-state energy. All final states accessed through the EDC peaks at various photon energies in (a) are marked by red crosses. Arrows on the vertical axis mark final-state band gaps. (d) The initial-state k_z dispersion of (b) is replotted by interchanging the horizontal and vertical scales for ease of identifying the final states corresponding to EDC peaks in (a). Vertical line shows how the initial state related to the specific EDC peak marked by the red cross connects with the final state. (e) Spectral feature at zero binding energy due to the Dirac cone in (a) is shown on an enlarged scale in order to highlight details of intensity variations with photon energy.

the $\bar{\Gamma}\bar{M}$ direction. Peaks in the EDCs give binding energies of various *initial-state* Bloch levels at this $k_\parallel$ value; changes in the position of a peak with photon energy reflect how the binding energy of the associated initial state disperses with k_z, the component of its Bloch momentum perpendicular to the surface. The peak at zero binding energy comes from the Dirac cone state at the E_F. The binding energy of this peak does not change with $h\nu$ because the associated surface state, which is localized in the z direction, does not disperse with k_z. The other peaks in Fig. 2(a) result from bulk levels, which generally disperse with $h\nu$ [28]. In fact, even though only the $k_\parallel$ value is fixed, the binding energy of an EDC peak also implies a specific value of k_z. This is illustrated in Fig. 2(b), which shows the k_z dispersion of the initial state associated with the marked peak (red cross) in the EDC for $h\nu = 7.7$ eV, and the k_z value that corresponds to its binding energy [29]. Movements in positions of peaks in the EDCs thus probe k_z dispersion of the initial-state bands.

Turning next to the final states, as Figs. 2(c) and 2(d) show, the final state for a given initial state can be obtained by adding $h\nu$ to its energy, while keeping k_z unchanged because the momentum of the photon is negligible for laser or UV photoemission [30]. Note that in Figs. 2(c) and 2(d), the horizontal scale gives k_z, and that Figs. 2(b) and 2(d) are the same, except that the horizontal and vertical axes are interchanged. In this way, we have analyzed all the bulk peaks in the EDCs of Fig. 2(a), and all final states so accessed in Bi_2Te_3 via photon energies of 5.5–12.9 eV are marked with red crosses in Fig. 2(c). Not all available final states are accessible due to constraints of energy and momentum conservation, and the effects of the ARPES matrix element, which connects the initial and final states in the photoemission process. The pattern of red crosses is interrupted by gaps around $k_z = 0$ for final-state energies just below 5.9 eV and around 6.4 eV and 8.4 eV; this is also the case around 11.4 eV at $k_z \approx 0.15$ near the band edge. [The final-state band gaps are marked by arrows on the vertical scale in Fig. 2(c).] These gaps influence the EDCs in an important way in that the spectral intensities for photon energies which involve connecting to final states in these energy-momentum regions are greatly attenuated. This is the reason behind the regions of highly reduced spectral intensities seen around photon energies of 5.9, 6.5, 8.5, and 11.5 eV in the EDCs of Fig. 2(a).

We comment on how the spectral intensities of the Dirac cone states are affected by the final-state gap structure with reference to Fig. 2(e), which gives an enlarged plot of the EDCs of Fig. 2(a) around the zero binding energy region corresponding to emission from the Dirac cone. The key difference in the way the bulk and Dirac states probe the final-state gaps is related to the nature of their k_z dispersions: bulk states have finite k_z dispersions as seen in Fig. 2(b), while the Dirac states, being localized in the direction perpendicular to the surface, have no k_z dispersion. As a result, the final-state gaps probed via bulk emission are localized in momentum (k_z)

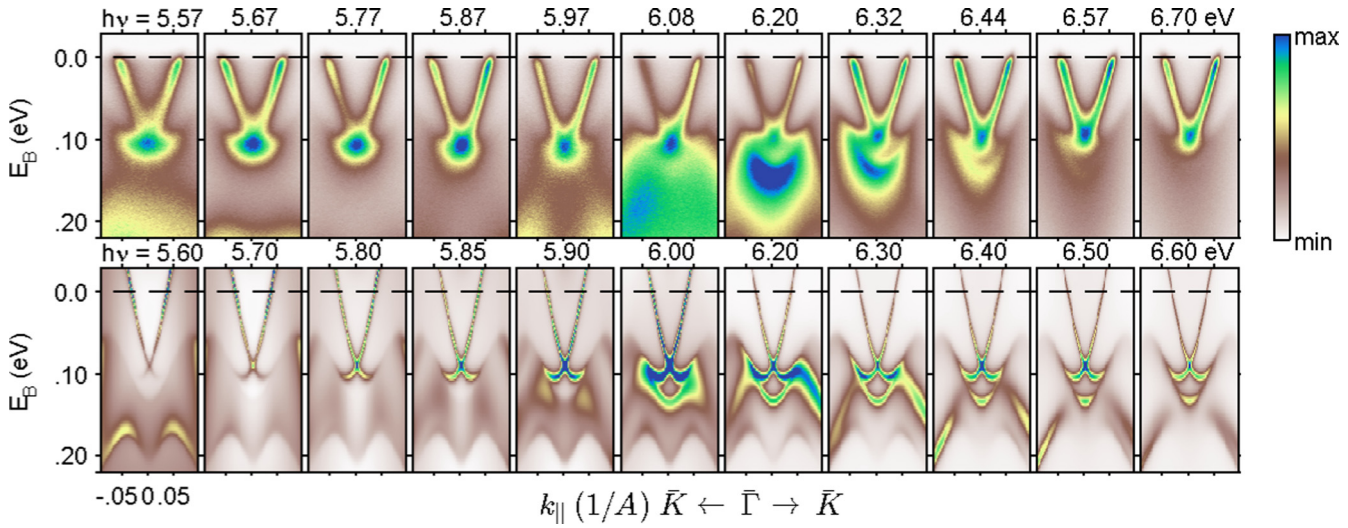

FIG. 3. Same as the caption to Fig. 1, except that the experimental (top row) and computational (bottom row) spectra are taken along the $\bar{\Gamma}\bar{K}$ direction; properties of the incoming light are also similar, except that the propagation direction is along $\bar{\Gamma}\bar{M}$.

space, but in sharp contrast, emission from Dirac cone states is insensitive to k_z, and it is attenuated substantially only if the final-state gap extends over all k_z values. This is the reason behind the low spectral intensity for emission from the bulk as well as Dirac states at $h\nu = 5.5$ eV in Figs. 2(a) and 2(e). On the other hand, the 8.4 eV final-state gap is 470 meV around $k_z = 0$ and leads to substantial suppression of bulk emissions in Fig. 2(c), but the corresponding gap when all k_z values are considered is only 150 meV, which is of the order of the final-state width of 200 meV used in the computations, and thus yields little effect on the Dirac cone intensity around 8.5 eV photon energy in Fig. 2(e).

We return now to comment further on the results of Fig. 1. Through an analysis of the spectra of Fig. 1 along the lines of Fig. 2 above, we adduce that upward/downward movements in the bulk intensity around the Dirac node in Fig. 1 reflect effects of k_z dispersion of the initial states. Note that the scale of these movements is of the order of ± 0.1 eV as is to be expected from the typical initial-state k_z dispersion in Bi_2Te_3; see Fig. 2(b). On the other hand, suppression of spectral intensity originates from gaps in the underlying final-state spectrum. This is seen to be the case in the experimental spectra of Fig. 1 (top row) around 5.77 and 6.44 eV photon energies, in reasonable accord with the presence of theoretical final-state gaps in Bi_2Te_3 around 5.9 and 6.4 eV.

We emphasize that rapid variations in spectral intensities with photon energy such as those seen in Fig. 1, which are driven by the small underlying initial-state k_z dispersions and final-state gaps of the order of 0.1 eV, would be washed out in UV photoemission where the final-state dampings are of the order of 1 eV [31]. Longer lifetimes of the final states in laser-ARPES can be expected since the energies of photoemitted electrons typically lie below the threshold for the onset of plasmon excitations [32]. Our study thus shows that laser-ARPES can effectively probe subtle features of both the initial and final-state band structure [33]. The value of laser-ARPES as a unique window on delicate final-state features has previously been noted in connection with the initial states [34] only.

In Fig. 3, experimental ARPES intensities are compared with the corresponding computations for momenta along the $\bar{\Gamma}\bar{K}$ direction. By considering a different momentum cut than that in Fig. 1 allows us to expand the range of data over which theory and experiment are compared, providing a greater

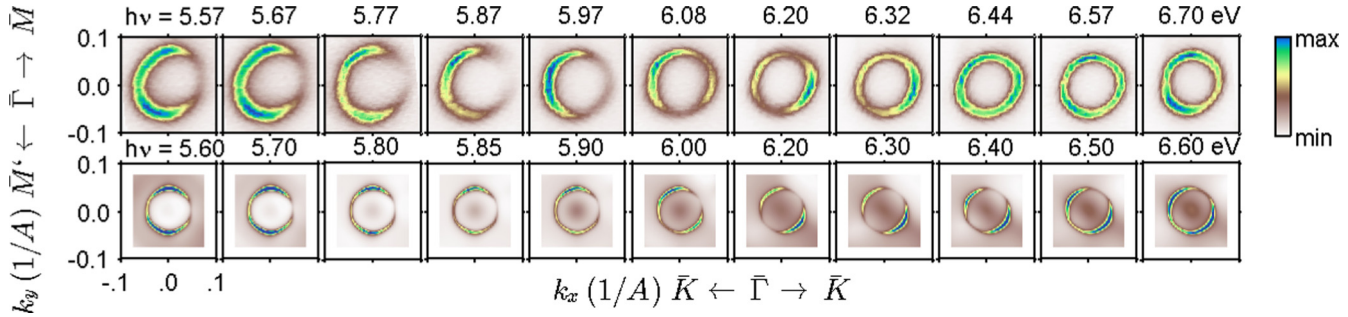

FIG. 4. Same as the caption to Fig. 1, except that instead of the energy vs momentum cuts of Fig. 1, here spectral intensities for photoemission from the Fermi energy are shown in the $\bar{\Gamma}\bar{K} - \bar{\Gamma}\bar{M}$ momentum plane for various photon energies. Experimental spectra (top row) have been rotated anticlockwise by 5° to account for the misalignment of the experimental spectra with respect to $\bar{\Gamma}\bar{K}$. Fermi energy in the computations has been chosen to obtain a reasonable accord between the sizes of the experimental and theoretical Fermi surfaces associated with the Dirac cone states.

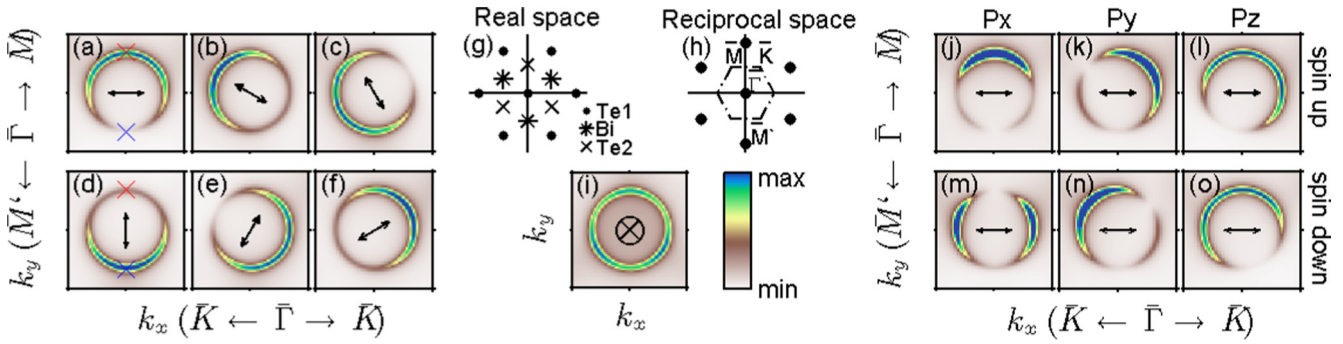

FIG. 5. (a)–(f) Theoretical photointensities for emission from the Fermi energy in Bi_2Te_3 for light incident normal to the surface ($h\nu = 9.6$ eV) with various directions of the in-plane polarization vector, shown by the double arrows; the out-of-plane component of the polarization vector is zero. The k points marked with red and blue crosses in (a) and (d) are discussed in the text. (g) Top view of the crystal surface with Te atoms (filled circles) in the topmost layer. Bi atoms (stars) lie in the second layer, followed by another layer of Te atoms (crosses). (h) Reciprocal lattice points are shown along with the first Brillouin zone and a few high-symmetry points. (i) Same as (a)–(f), except that the light here is incident horizontally, so that the polarization vector lies normal to the surface with no in-plane component. (j)–(l) Spin-up component of the intensity for electron spin polarized along the x, y, and z directions, respectively. Incident light polarization is the same as in (a). (m)–(o) Same as (j)–(l), except these panels give the corresponding spin-down intensities.

degree of confidence in our modeling and interpretation of the spectra. Here again, like in Fig. 1, experimental spectra show bulk band-gap-related emissions for $h\nu = 5.77$ and 6.44 eV, initial state k_z dispersion driven movements in bulk features around the Dirac node, and some signatures of final-state band gaps in emission from the Dirac cone states. All of these observed features are captured reasonably by the computations [35]. Notably, in the small energy range over which the Dirac states are probed in the present study, the hexagonal warping effects are quite small and would not be accessible within our experimental resolution.

Figure 4 considers emissions from E_F in the $k_x - k_y$ momentum plane. The Fermi surface (FS) obtained by cutting the Dirac cone is of course circular, but the spectral intensities in the imprints of the FS in Fig. 4 are seen to be highly modulated via effects of the ARPES matrix element, which depend strongly on the photon energy. In particular, in going from the lowest to the highest photon energies in the experimental spectra of Fig. 4 (top row), we see the following: at $h\nu = 5.57$ eV, the FS contour shows a region of minimum intensity along the (horizontal) $\bar{\Gamma}\bar{K}$ direction for $k_x > 0$; this region of small spectral intensity spreads out and extends over nearly half the FS by 5.97 eV; spectral intensity then begins to reappear in the low-intensity region and, by $h\nu = 6.20$ eV, the FS imprint consists of two regions of low intensity; and, with further increase in the photon energy, the FS contour begins to fill up again. This characteristic evolution of the FS imprint is essentially reproduced by the computations in the lower row of the figure. We note that the measured shape of the FS deviates from circular for low phonon energies. This is most likely caused by small distortions of the photoelectrons for low kinetic energies.

Simulations of Fig. 5 give insight into the symmetry characteristics of emissions from the Dirac cone when the polarization vector of the incoming light is varied systematically. Although our modeling properly includes spin textures of the Dirac states and the spin polarization of the outgoing electrons, we first focus on symmetries underlying the spin-independent spectra. For light incident normally, Figs. 5(a)–5(f) show that as the in-plane polarization vector is rotated clockwise, the spin-independent intensity pattern rotates in the opposite (counterclockwise) direction. More specifically, when the polarization vector is rotated clockwise by 30° in going from Fig. 5(a) to 5(b), the mirror plane which was vertical in Fig. 5(a) has rotated anticlockwise by 60°. Similarly, a 90° rotation of the polarization vector causes a 180° rotation of the intensity pattern, but the mirror plane involved remains the same, as seen by comparing Figs. 5(a) and 5(d), or 5(b) and 5(e), or 5(c) and 5(f). For light polarized along $\bar{\Gamma}\bar{M}$, the intensity pattern reveals a mirror plane parallel to the polarization vector as seen in Figs. 5(b), 5(d), and 5(f). In contrast, for light polarized along $\bar{\Gamma}\bar{K}$, the mirror plane lies perpendicular to the polarization vector; see Figs. 5(a), 5(c), and 5(e). This alternation between the parallel and perpendicular mirror planes is responsible for driving the unexpected (counterclockwise) rotation of the intensity pattern with (clockwise) rotation of the in-plane polarization vector and reflects the symmetry properties of the ARPES matrix element. Maximum symmetry is revealed for grazing incidence of the incoming light; see Fig. 5(i). Here, the polarization vector has zero in-plane component, and the emission pattern displays the full threefold symmetry of the lattice within the precision of our computations.

Figures 5(j)–5(o) turn to consider an example of spin-dependent spectra and show spin-up (top row) and spin-down (bottom row) components of the intensity for electron spin polarized along the x, y, and z directions, respectively, where the incident light is polarized horizontally as in Fig. 5(a). For electron spin polarized along x, the intensity patterns in Figs. 5(j) and 5(m) for the up- and down-spin components, respectively, are left-right symmetric. This symmetry reflects the presence of a vertical mirror plane perpendicular to the (horizontal) light polarization as in Fig. 5(a). However, when the electron is polarized along y [Figs. 5(k) and 5(n)] or along z [Figs. 5(l) and 5(o)], we no longer have this mirror plane and the left-right symmetry of the intensity pattern is broken. Results of Fig. 5 suggest that insight into the spin textures of the Dirac states could be obtained through

an analysis of the polarization dependence of the ARPES spectra, although further work is needed to unfold the precise nature of the connection between the spin textures and helicity of the Dirac states and the spin dependencies of the associated ARPES spectra. In this way, it may be possible to identify experimental phase-space regions (photon energies and polarizations), which would be favorable for zooming in on specific aspects of spin textures of Dirac states.

It is interesting to recall that the ARPES matrix element involves the matrix element $\langle i|A.p|f\rangle$ of the dipole operator, where $|i\rangle$ and $|f\rangle$ are the initial- and final-state wave functions, A is the vector potential of the incident light field, and p is the electron momentum operator. Consider now the intensity plots of Figs. 5(a) and 5(d), which as we have already noted must be left-right symmetric due to the presence of the vertical mirror plane in the lattice, and this symmetry is not broken by the incident light field. Focus on the momentum point k_{red}, marked by the red cross in the mirror plane in Fig. 5(a). Since the final-state wave function must be even in the mirror plane (otherwise there will be no outgoing electrons) and the dipole operator is odd, the initial state at k_{red} must have a finite odd component to yield a nonzero value of the intensity. On the other hand, if we consider the same k point in Fig. 5(d) where the dipole matrix element is even with respect to the vertical mirror plane, we see immediately that now we must have a finite even component to obtain nonzero intensity, as is seen to be the case. [Arguments along the preceding lines can be made to gain insight into the symmetry properties of the initial-state wave function at the k point, k_{blue}, marked with a blue cross in Figs. 5(a) and 5(d).]

V. SUMMARY AND CONCLUSIONS

We have carried out laser-ARPES measurements over the photon energy range of 5.57–6.70 eV on oriented single crystals of Bi_2Te_3, along with parallel, fully relativistic, first-principles computations of the ARPES spectra within the one-step model of photoemission. Spectra for light polarized linearly along two different directions, which are essentially the $\bar{\Gamma}\bar{M}$ and the $\bar{\Gamma}\bar{K}$ directions, are considered. Theory is shown to reproduce characteristic features of the experimental spectra, and their observed evolution with photon energy. We identify signatures of final-state gaps in the Dirac cone emissions, and show why these signatures are more subtle than those in the bulk spectra, and how insight into the spin textures of Dirac cone states could be obtained through the polarization dependencies of the spectra. Our study demonstrates that laser-ARPES is not only a sensitive probe of the k_z dispersion of the bulk (initial) states, but that these spectra can also provide a window for mapping small, momentum-dependent gaps in the final-state band structure.

ACKNOWLEDGMENTS

The computational part of this work at Tampere University of Technology benefited from the grid computing software provided by Techila Technologies Ltd. The work at Northeastern University was supported by the U.S. Department of Energy (DOE), Office of Science, Basic Energy Sciences Grant No. DE-FG02-07ER46352 (core research), and benefited from Northeastern University's Advanced Scientific Computation Center (ASCC), the NERSC supercomputing center through the U.S. DOE Grant No. DE-AC02-05CH11231, and support (applications to layered materials) from the U.S. DOE EFRC: Center for the Computational Design of Functional Layered Materials (CCDM) under Grant No. DE-SC0012575. The work at Ames Laboratory (ARPES measurements, materials synthesis, and data analysis) was supported by the U.S. Department of Energy, Office of Science, Basic Energy Sciences, Materials Science and Engineering Division. Ames Laboratory is operated for the U.S. Department of Energy by Iowa State University under Contract No. DE-AC02-07CH11358.

[1] We refer to Refs. [2–14] below for extensive reviews of the literature and discussion of various aspects of topological materials.
[2] A. Bansil, H. Lin, and T. Das, Rev. Mod. Phys. **88**, 021004 (2016).
[3] X.-L. Qi and S.-C. Zhang, Rev. Mod. Phys. **83**, 1057 (2011).
[4] M. Z. Hasan and C. L. Kane, Rev. Mod. Phys. **82**, 3045 (2010).
[5] W. Feng and Y. Yao, Sci. Chin. Phys. Mech. Astron. **55**, 2199 (2012).
[6] B. Yan and S.-C. Zhang, Rep. Prog. Phys. **75**, 096501 (2012).
[7] Y. Ando, J. Phys. Soc. Jpn. **82**, 102001 (2013).
[8] J. H. Bardarson and J. E. Moore, Rep. Prog. Phys. **76**, 056501 (2013).
[9] C. Beenakker, Ann. Rev. Condens. Matter Phys. **4**, 113 (2013).
[10] M. Dzero, K. Sun, V. Galitski, and P. Coleman, Phys. Rev. Lett. **104**, 106408 (2010).
[11] M. Fruchart and D. Carpentier, C. R. Phys. **14**, 779 (2013).
[12] T. Okuda and A. Kimura, J. Phys. Soc. Jpn. **82**, 021002 (2013).
[13] H. Zhang and S.-C. Zhang, Phys. Status Solidi Rapid Res. Lett. **7**, 72 (2013).
[14] T. Wehling, A. Black-Schaffer, and A. Balatsky, Adv. Phys. **63**, 1 (2014).
[15] M. R. Scholz, J. Sánchez-Barriga, J. Braun, D. Marchenko, A. Varykhalov, M. Lindroos, Y. J. Wang, H. Lin, A. Bansil, J. Minár, H. Ebert, A. Volykhov, L. V. Yashina, and O. Rader, Phys. Rev. Lett. **110**, 216801 (2013).
[16] M. Neupane, S. Basak, N. Alidoust, S.-Y. Xu, C. Liu, I. Belopolski, G. Bian, J. Xiong, H. Ji, S. Jia, S.-K. Mo, M. Bissen, M. Severson, H. Lin, N. P. Ong, T. Durakiewicz, R. J. Cava, A. Bansil, and M. Z. Hasan, Phys. Rev. B **88**, 165129 (2013).
[17] T. L. Miller, M. Arrala, C. L. Smallwood, W. Zhang, H. Hafiz, B. Barbiellini, K. Kurashima, T. Adachi, Y. Koike, H. Eisaki, M. Lindroos, A. Bansil, D.-H. Lee, and A. Lanzara, Phys. Rev. B **91**, 085109 (2015).
[18] A. Bansil and M. Lindroos, Phys. Rev. Lett. **83**, 5154 (1999).
[19] S. Sahrakorpi, M. Lindroos, R. S. Markiewicz, and A. Bansil, Phys. Rev. Lett. **95**, 157601 (2005).

[20] V. Arpiainen, A. Bansil, and M. Lindroos, Phys. Rev. Lett. **103**, 067005 (2009).
[21] J. Braun, Rep. Prog. Phys. **59**, 1267 (1996).
[22] J. Pendry, Surf. Sci. **57**, 679 (1976).
[23] C. Caroli, D. Lederer-Rozenblatt, B. Roulet, and D. Saint-James, Phys. Rev. B **8**, 4552 (1973).
[24] V. N. Strocov, R. Claessen, and P. Blaha, Phys. Rev. B **68**, 144509 (2003).
[25] M. Ärrälä, J. Nieminen, J. Braun, H. Ebert, and M. Lindroos, Phys. Rev. B **88**, 195413 (2013).
[26] E. D. L. Rienks, M. Ärrälä, M. Lindroos, F. Roth, W. Tabis, G. Yu, M. Greven, and J. Fink, Phys. Rev. Lett. **113**, 137001 (2014).
[27] Various spectral features are seen to be sharper in the computed spectra compared to the corresponding experimental features in Figs. 1, 3, and 4. We have done so deliberately by invoking a small damping parameter for the initial states in order to more clearly identify various features in the computed spectra.
[28] Nondispersing density-of-states-type bulk features arise from the band edges of the initial-state bands; an example is the feature at 0.1eV binding energy in Fig. 2(a) [36] .
[29] Note that a given binding energy in Fig. 2(b) will generally yield two distinct values of k_z. However, only one of these two k_z values is physically relevant for the photoemission process because the state with the other k_z involves an electron directed into the crystal surface .
[30] Red crosses in Fig. 2(c) give real parts of the eigenvalues for an effective Hamiltonian in which a complex self-energy correction has been added to the crystal potential. Such solutions are then found at all energies, but disperse rapidly in the band gaps with large imaginary parts or dampings, indicating a lack of propagating solutions [37]. See Ref. [38] for further discussion.
[31] Note that a large final-state width generally has little affect on the width of the initial-state spectral peaks [38]; see Ref. [38] for discussion.
[32] L. Hedin and S. Lundqvist, *Solid State Physics, Advances in Research and Applications*, edited by F. Seitz, D. Turnbull, and H. Ehrenreich, Vol. 23 (Academic, New York, 1969).
[33] We did not attempt a quantitative comparison between theory and experiment, which would require greater attention to details such as the intrinsic doping level of the Dirac cone states in the Bi2Te3 sample measured, specifics of the initial- and final-state damping parameters used in the modeling of Dirac and bulk states, and details of the surface-barrier potentials.
[34] J. D. Koralek, J. F. Douglas, N. C. Plumb, Z. Sun, A. V. Federov, M. M. Murnane, H. C. Kapteyn, S. T. Cundiff, Y. Aiura, K. Oka, H. Eisaki, and D. S. Dessau, Phys. Rev. Lett. **96**, 017005 (2006).
[35] Slight asymmetry of spectral intensities seen in experiment as well as theory in Fig. 3 with respect to $\bar{\Gamma}$ is due to small misalignment of the sample.
[36] M. Lindroos and A. Bansil, Phys. Rev. Lett. **77**, 2985 (1996).
[37] S. Davison and M. Steslicka, *Basic Theory of Surface States* (Oxford University Press, Oxford, 1992).
[38] P. Thiry, D. Chandesris, J. Lecante, C. Guillot, R. Pinchaux, and Y. Petroff, Phys. Rev. Lett. **43**, 82 (1979).